

Predicting survival outcomes using topological features of tumor pathology images

Chul Moon^{*1}, Qiwei Li², and Guanghua Xiao³

¹Department of Statistical Science, Southern Methodist University, Dallas, TX, USA

²Department of Mathematical Science, University of Texas at Dallas, Richardson, TX, USA

³Department of Population & Data Sciences and Department of Bioinformatics, University of Texas Southwestern Medical Center, Dallas, TX, USA

Abstract

Tumor shape and size have been used as important markers for cancer diagnosis and treatment. Recent developments in medical imaging technology enable more detailed segmentation of tumor regions in high resolution. This paper proposes a topological feature to characterize tumor progression from digital pathology images and examine its effect on the time-to-event data. We develop distance transform for pathology images and show that a topological summary statistic computed by persistent homology quantifies tumor shape, size, distribution, and connectivity. The topological features are represented in functional space and used as functional predictors in a functional Cox regression model. A case study is conducted using non-small cell lung cancer pathology images. The results show that the topological features predict survival prognosis after adjusting for age, sex, smoking status, stage, and size of tumors. Also, the topological features with non-zero effects correspond to the shapes that are known to be related to tumor progression. Our study provides a new perspective for understanding tumor shape and patient prognosis.

Keywords: Non-small Cell Lung Cancer, Persistent Homology, Prognosis, Topological Data Analysis, Tumor Shape

^{*}Corresponding author. Email: chulm@smu.edu

1 Introduction

Recent advancements in the field of medical image analysis lead to a high-resolution and informative description of human cancer. With such developments, medical images have a significant influence on medical decision making. Radiomics has been developed for decision support by extracting quantitative features of images and providing data for further analyses (Gillies et al., 2016; Rizzo et al., 2018). The two of the most common types of features are texture and shape (Bianconi et al., 2018). The textural features summarize the area, kurtosis, entropy, and correlation computed from pixel intensity and the gray-level co-occurrence matrix (Haralick et al., 1973). The shape features mainly focus on the boundaries of segmented tumor regions and quantify their roughness or irregularities. The existing shape features include the curve-based approach (Bharath et al., 2018), fractal analysis (Brú et al., 2008; Lopes et al., 2011), geometric and radial boundary descriptors (Kilday et al., 1993; Rangayyan et al., 1997), landmark points (Bookstein, 1997; Dryden and Mardia, 2016), and topological summary (Crawford et al., 2020). However, the existing tumor shape features do not summarize detailed local patterns such as a relationship between tumor and normal regions, distribution, and connectivity. Also, the features developed to deal with radiographic images could be inadequate in high-resolution pathology images (Madabhushi and Lee, 2016). In this paper, we propose using topological features to quantify various aspects of shapes in pathology image using persistent homology.

Topological data analysis is a recently emerged area of study that investigates the shape of data using their topological features. Persistent homology is a commonly used topological data analysis tool that analyzes the shape of data with the multi-scale topological lens (Edelsbrunner and Harer, 2008; Carlsson, 2009). Persistent homology provides a numeric summary of the shape that is robust to noise and insensitive to metrics (Chazal et al., 2017). Persistent homology has been applied to tumor image analyses such as colorectal tumor region segmentation (Qaiser et al., 2016), clustering of Gleason score of prostate cancer histology (Lawson et al., 2019; Berry et al., 2020), and hepatic tumor classification (Oyama et al., 2019). However, the topological features in the previous studies are closer to the textural features than the shape features. This paper applies persistent homology to pathology images and reveals various information on size, shape, distribution, and connectivity of tumor and normal regions.

We can conduct statistical inference on different patterns in pathology images using the topological features computed by persistent homology. However, persistent homology results cannot be used as predictors in most statistical models; 1) numeric outputs of persistent homology are sets of intervals that are not vectors, and 2) the number of intervals generated is different from dataset to dataset. Several methods have been suggested to represent persistent homology results in different spaces, including Euclidean space (Bendich et al., 2016; Adams et al., 2017), functional space (Chen et al., 2015; Bubenik, 2015; Berry et al., 2020) and reproducing kernel

Hilbert space (Reininghaus et al., 2015; Kusano et al., 2016). We represent persistent homology results in functional spaces and implement them in a survival model as functional predictors.

We consider the functional Cox regression (FCR) model to characterize the association between topological features and survival outcomes. Since Chen et al. (2011) propose the FCR model, various approaches have been developed; using the penalized partial likelihood (Gellar et al., 2015), Bayesian modeling (Lee et al., 2015), the optimal rate of convergence (Qu et al., 2016), functional principal components (Kong et al., 2018), and penalized semiparametric inference (Hao et al., 2020). In our study, the FCR model of Kong et al. (2018) is extended to include the multiple functional predictors obtained by persistent homology. We conduct a case study on lung cancer pathology images. The result shows that the functional predictors are associated with patient survivals, and the discovered topological features coincide with the tumor progression. The proposed method enables in-depth shape analysis on the survival prognosis using topological features of pathology images.

The rest of the paper is organized as follows. Section 2 introduces persistent homology and topological features of pathology images as well as their functional representations. Section 3 describes the FCR model. In Section 4, we show an application to lung cancer image data. Section 5 concludes the paper and discusses future research topics.

2 Shape Analysis for Pathology Images using Topology

2.1 Homology and Persistent Homology

Consider a shape is given as a topological space \mathcal{S} . Homology studies geometric patterns of \mathcal{S} by examining its k -dimensional holes. For example, zero-dimensional holes are connected components, one-dimensional holes are loops, and two-dimensional holes are voids. These k -dimensional holes are often called the topological features of the shape. Let $H_k(\mathcal{S})$ denotes the k -th homology group of \mathcal{S} . The Betti number β_k is the rank of $H_k(\mathcal{S})$ and it counts the number of k -dimensional holes in \mathcal{S} . Figure 1 present three topological spaces and their Betti numbers.

Computing homology of topological space is challenging, albeit its simple concept. To overcome the computational issue, a topological space S is often approximated as a simplicial complex K . The simplicial complex is a finite set of simplices glued together. Examples of simplices are a point (0-simplex), line (1-simplex), triangle (2-simplex), and tetrahedron (3-simplex). The discretized representation of shape enables computationally efficient homology computation (Edelsbrunner and Harer, 2008).

Persistent homology provides multi-scale homology representation of topological spaces. Let $\emptyset \subseteq K_0 \subseteq K_\epsilon \subseteq \dots \subseteq K_N$ be a non-decreasing sequence of simplicial complexes. Here, the inclusion \subseteq implies that a set of simplices on the left side of \subseteq is included on the right side of the simplicial complex. The index ϵ that controls the sequence is called the filtration. Figure 2

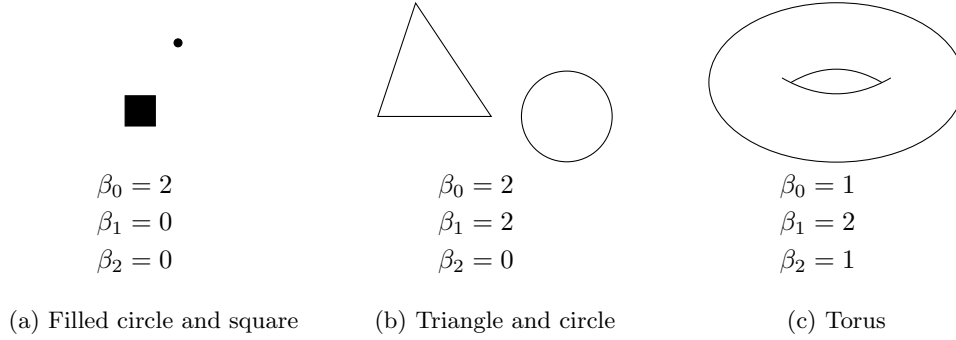


Figure 1: Topological space examples and their Betti numbers. β_0 , β_1 , and β_2 represent the number of zero, one, and two dimensional holes. For example, the triangle in Figure 1b is one connected component with one hole ($\beta_0 = 1$ and $\beta_1 = 1$). Similarly, the Betti numbers of the circle in Figure 1b is $\beta_0 = 1$ and $\beta_1 = 1$. Therefore, the Betti numbers of Figure 1b is $\beta_0 = 2$ and $\beta_1 = 2$.

presents a sequence of simplicial complexes with four vertices at $(0, 0)$, $(1, 0)$, $(1, 1)$, and $(0.4, 1)$. In K_ϵ , a $(k - 1)$ -simplex is constructed if all pairwise distances between k vertices are less than or equal to ϵ . We see that homology evolves as the filtration value ϵ increases. For example, the 0-th Betti number of K_0 is $\beta_0 = 4$ as it has four disconnected points. On the other hand, $\beta_0 = 3$ in $K_{0.6}$ as the two points are connected.

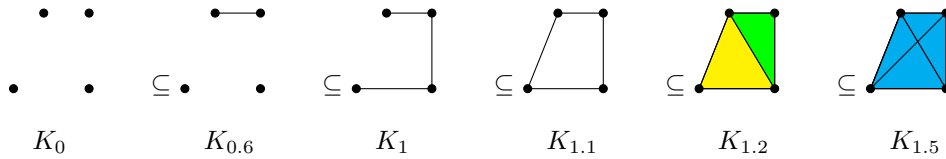


Figure 2: Sequence of simplicial complexes. In K_ϵ , $k - 1$ -simplex if all pairwise distances between k vertices are less than or equal to ϵ . The dots and lines are vertices (0-simplices) and edges (1-simplices), respectively. The yellow- and green-colored regions in $K_{1.2}$ are triangles (2-simplices), and the blue-colored region in $K_{1.5}$ is a tetrahedron (3-simplex). Figures will appear in color in the electronic version of this article.

Persistent homology observes the evolution of homology. The inclusion of K_i in K_j for $0 \leq i \leq j \leq N$ induces a map between the homology groups so that

$$0 \rightarrow H(K_0) \rightarrow H(K_1) \rightarrow \cdots \rightarrow H(K_N).$$

The image of the map between homology groups includes information when a specific k -dimensional hole appears (birth) and disappears (death) over the filtration. Persistent homology computation result is given as multiple intervals of (birth, death). The length of the interval (death–birth) shows how long the topological feature persists. For example, persistent homology computation

output for $0 \leq \epsilon \leq 1.5$ of Figure 2 is four intervals for dimension zero, $(0, 0.6)$, $(0, 1)$, $(0, 1)$, and $(0, 1.5)$, and one interval for dimension one, $(\sqrt{1.16}, \sqrt{1.36})$.

A persistence diagram is a collection of points in \mathbb{R}^2 where points in the diagram represent the birth and death values of features. Let $P = \{(b, d) \in \mathbb{R}^2 : b < d\}$ be a persistence diagram such that (b, d) denotes the birth and death values and \mathcal{D} be the space of persistence diagrams. The birth and death values can be plotted as points on the horizontal and vertical axis, respectively. Because the death of a topological feature comes after its birth, points are placed above the diagonal line. The persistent homology computation results of Figure 2 are illustrated as persistence diagrams in Figure 3.

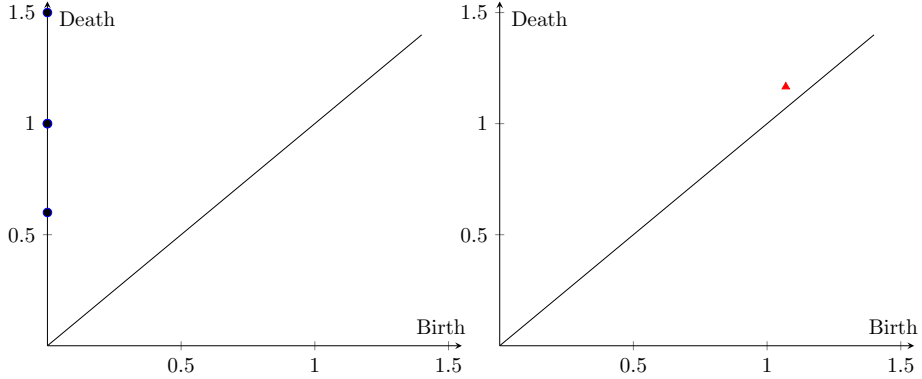


Figure 3: Dimension zero persistence diagram (left) and dimension one persistence diagram (right) of the simplicial complexes in Figure 4.

2.2 Persistent Homology Transform and Smooth Euler Curve Transform

The persistent homology transform (PHT) is a recent addition to the topological shape analysis toolbox proposed by Turner et al. (2014). The PHT provides a detailed summary of shapes by sweeping their sub-level sets in different directions. For a shape in two- and three-dimensional spaces, a one-to-one relationship is guaranteed between the shapes and their PHT computation results (Turner et al., 2014). Consider a simplicial complex of interest K in \mathbb{R}^d . The sweeping direction ν can be expressed as a point in a unit $(d - 1)$ -sphere, $\nu \in S^{d-1}$. Let $K_{(\nu, \epsilon)}$ be the sub-level complex that includes all simplices below the height ϵ along the direction ν . For a given direction and orientation, persistent homology is computed using the height as a filtration, $h_{\min} \leq \epsilon \leq h_{\max}$, where h_{\min} and h_{\max} are range of filtration that can include all simplices in $K_{(\nu, \epsilon)}$. The process is repeated over infinitely many directions in S^{d-1} and the shape is summarized as a collection of persistence diagrams. In real applications, a large enough number of directions are selected. PHT can be defined as a function $\text{PHT}(K) : S^{d-1} \rightarrow \mathcal{D}^d$.

The Euler characteristic curve transform (ECT) is a simple extension of the PHT. The Euler characteristic is a commonly used value to examine the topological properties as a single integer. The Euler characteristic of topological space \mathcal{S} is $\chi(\mathcal{S}) = \beta_0 - \beta_1 + \beta_2 + \dots = \sum_{i=0}^{\infty} (-1)^i \beta_i$, where β_i is i -th Betti number of \mathcal{S} . The ECT generates a set of Euler characteristic curves, similar to a set of persistence diagrams in the PHT. We denote $\chi(K_{(\nu,\epsilon)}) \in \mathbb{Z}$ as the Euler characteristic curve that tracks evolution of the Euler characteristic for a given sweeping direction ν , orientation, and the filtration from h_{\min} to h_{\max} . The Euler curve transform (ECT) collects the Euler characteristic curve from all directions and can be defined as a function $\text{ECT}(K) : S^{d-1} \rightarrow \mathbb{Z}^{\mathbb{R}}$. Because the Euler characteristic is the alternating sum of the rank of the homology group, the ECT is also an injective function. Crawford et al. (2020) propose the smooth Euler characteristic curve transform (SECT) that computes the centered and cumulative Euler characteristic curve by subtracting the mean from the Euler characteristic curve, $\chi(K_{(\nu,\epsilon)}) - \bar{\chi}(K_{(\nu,\epsilon)})$. The SECT collects a set of functions in Hilbert space, $\text{SECT}(K) : S^{d-1} \rightarrow \mathbb{L}^2[h_{\min}, h_{\max}]$.

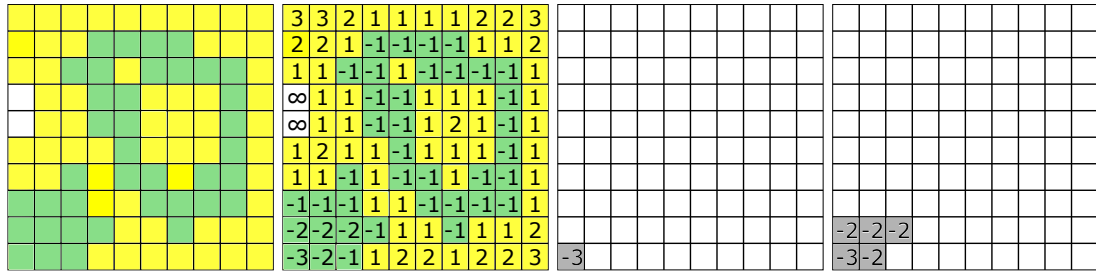
2.3 Topological Features of Pathology Images

There are only a few studies that use topological features of pathology images to predict patient survival outcomes. Recently, Crawford et al. (2020) use the SECT to summarize the shape of the tumor boundary of glioblastoma multiforme and predict the survival prognosis using Gaussian process (GP) regression. Although their approach suggests that the summary of tumor shape paired with its location becomes useful, it comes with several limitations. First, the GP regression model cannot handle the right-censored datasets. Second, the SECT is sensitive to the rotation and orientation of images. This is challenging for some cases when pathology images do not have a pre-defined direction. Third, it is difficult to interpret the GP regression result and provide clinical implications. To overcome the challenges, we use persistent homology to describe the shape of pathology image data.

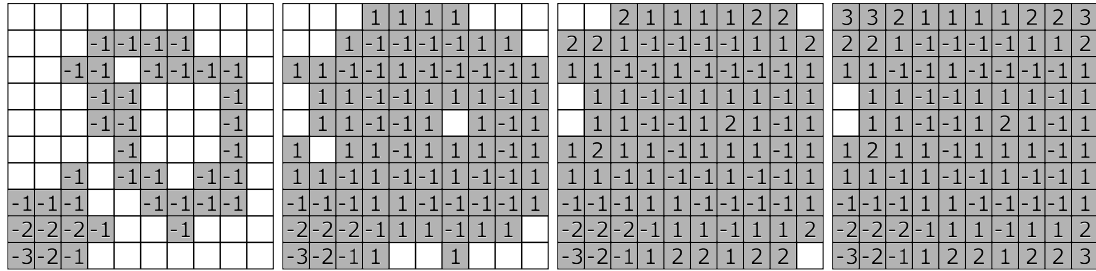
Persistent homology can reveal resourceful shape information when it is applied to image data. Robins et al. (2016) propose a signed Euclidean distance transform to reveal topological features for binary material images. It has been studied that persistent homology reveals pore structures and networks of three-dimensional material images (Robins et al., 2016; Herring et al., 2019; Moon et al., 2019).

Suppose that all pixels of pathology images are classified into one of the three classes: tumor, normal, and white (empty) regions. The three-class image itself does not reveal connectivity or size information. Structural and shape information can be discovered by using the distance transform. The signed Euclidean distance transform proposed by (Robins et al., 2016) cannot be used because it is developed for the binary images. We propose a signed Euclidean distance transform for the three-class pathology images (SEDT-3). The proposed SEDT-3 assigns the shortest Euclidean distance to the other classes to each pixel. The sign of the SEDT-3 value

depends on the classes; negative values for tumor region pixels, positive values for normal region pixels, and infinite values for the white region pixels. Figure 4a presents the three-class example image where the green-, yellow-, and white-colored pixels are tumor, normal, and white regions, respectively. Figure 4b shows the signed distance transformed values assigned for each pixel. Here, a taxicab metric is used instead of a Euclidean distance for convenience. We see that the signed distance values have shape information in the sense that it shows connectivity and adjacency relationships between the neighboring pixels.



(a) Three-class image (b) Signed distance (c) Cubical complex \mathcal{C}_{-3} (d) Cubical complex \mathcal{C}_{-2}



(e) Cubical complex \mathcal{C}_{-1} (f) Cubical complex \mathcal{C}_{-1} (g) Cubical complex \mathcal{C}_{-2} (h) Cubical complex \mathcal{C}_{-3}

Figure 4: (a): The three-class pathology image example. The green-, yellow-, and white-colored pixels are tumor, normal, and white regions, respectively. (b): Signed distances assigned to each pixel using the taxicab distance. (c)-(h): a sequence of cubical complexes based on the computed signed distance. The pixels included in the cubical complexes are marked in gray. Figures will appear in color in the electronic version of this article.

We construct a cubical complex using the distance transform values to compute persistent homology. The cubical complex is a set of multi-dimensional cubes, such as points, lines, squares, and cubes, that are glued together. The cubical complex allows describing a structure of an image while preserving its topology (Kovalevsky, 1989; Couprie et al., 2001). Let \mathcal{C}_ϵ be the cubical complex with filtration ϵ . In \mathcal{C}_ϵ , the pixels whose assigned distances are less than ϵ enter the complex. Figures from 4c to 4h present the sequence of cubical complexes with $\epsilon \in \{-3, -2, \dots, 3\}$.

We can obtain multi-scale shape information by tracking topological features of the sequence of cubical complexes. In Figure 4 example, two dimension zero features (connected components)

are recorded. The first dimension zero feature appears in \mathcal{C}_{-3} (bottom-left corner in Figure 4c) and the second dimension zero feature is created in \mathcal{C}_{-1} (middle in Figure 4e). Two components are connected in \mathcal{C}_1 so the second feature dies at $\epsilon = 1$. Also, we observe three dimension one features (loops) in the example. Two of them show up in \mathcal{C}_{-1} (two holes in the middle in Figure 4e). The smaller hole disappears in \mathcal{C}_1 and the larger hole is filled in \mathcal{C}_2 . The other dimension one component appears in \mathcal{C}_1 and disappears in \mathcal{C}_2 .

Persistent homology computes when topological features appear and disappear. The birth and death information of topological features explained above can be summarized in persistent diagrams in Figure 5. We want to note that the white region pixels do not enter in cubical complex because their distance transform values by the SEDT-3 are infinite. Therefore, the white region pixels do not directly affect persistent homology computation.

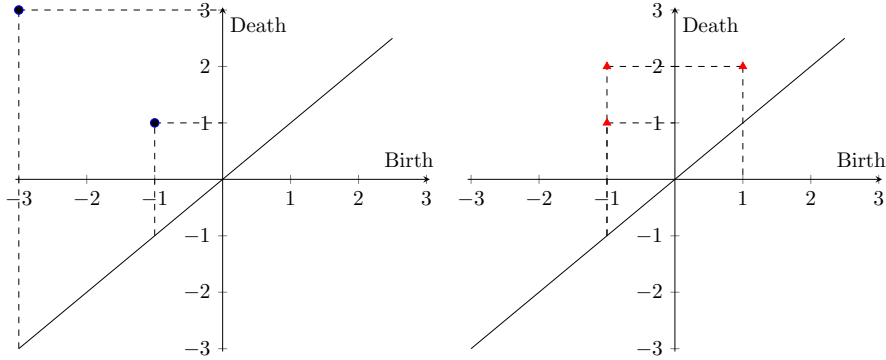


Figure 5: Dimension zero persistence diagram (left) and dimension one persistence diagram (right) of the cubical complexes from Figures 4c to 4h.

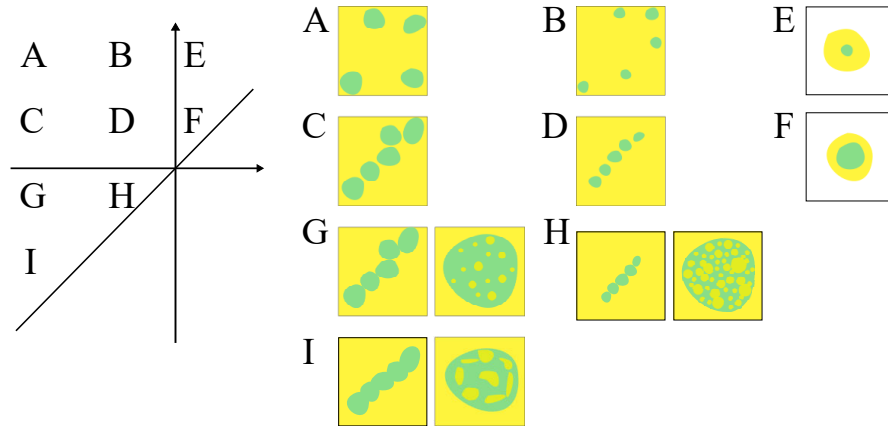
Various topological features of tumor pathology images can be summarized in different areas in persistence diagrams. Figure 6 illustrates the areas of dimension zero and one persistence diagrams and the corresponding example features.

Dimension zero features appear in the three non-zero quadrants of persistence diagrams: 1) quadrant II (e.g., A, B, C, and D); 2) quadrant I (e.g., E and F); and 3) and quadrant III (e.g., G, H, and I). First, the scattered tumors are recorded in quadrant II. The larger the tumor regions, the larger birth values are in quadrant II (e.g., A vs. B and C vs. D). Also, larger death values imply that distances between the disconnected tumor regions are far from each other (e.g., A vs. C and B vs. D). Second, quadrant I represents the separate normal regions that include tumor regions. Death values are proportional to the distance between the boundary of normal regions and the tumor regions inside (e.g., E vs. F). Third, connected tumor regions appear in quadrant III. The birth values are the size of tumor regions (e.g., G vs. H), and the death values are the size of the contact area of two tumor regions (e.g., G vs. I). The death value illustrates how close the tumor regions are. The connected tumor regions can be in different shapes. For example,

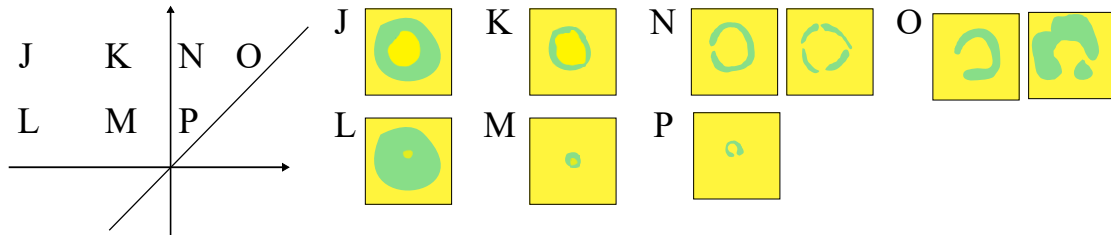
they could be a series of overlapped tumor regions (left figures of G, H, and I) or tumor regions that have normal regions inside (right figures of G, H, and I).

Dimension one features are summarized in two quadrants: 1) quadrant II (e.g., J, K, L, and M); and 2) quadrant I (e.g., N, O, and P). First, the normal regions surrounded by the tumor regions appear in quadrant II. Here, the large negative birth value means the surrounding tumor regions are thick (e.g., J vs. K and L vs. M), and the large death value means the trapped normal regions are large (e.g., J vs. L and K vs. M). Second, the broken-ring-shaped tumor regions are recorded in quadrant I. The large birth values imply that there are large gaps in the broken-ring shaped regions (e.g., N vs. O). Also, the large death value means the size of the inside of the broken-ring shape is large (e.g., N vs. P).

We note that the size of features is measured by the radius of the largest circle that can be placed inside of it. Also, dimension zero and one features are not exclusive; the pixels used to construct dimension zero features can be used to build dimension one feature and vice versa. For example, tumor regions in Figure 6b are also counted as dimension zero features.



(a) Dimension zero persistence diagram (left) and corresponding topological feature examples (right)



(b) Dimension one persistence diagram (left) and corresponding topological feature examples (right)

Figure 6: Topological features of three-class pathology images. The green, yellow, and white colored pixels are tumor, normal, and white regions, respectively. Figures will appear in color in the electronic version of this article.

2.4 Functional Representation of Topological Features

Although persistence diagrams include topological persistence signal information, it is not easy to use them directly as input in data analysis. This is because persistence diagrams are not in a common data type that most statistical models use. In our study, we represent persistence diagrams as persistence functions in a functional space inspired by Chen et al. (2015) and Adams et al. (2017).

We define the persistence function ρ_P of the persistence diagram P as

$$\rho_P(x, y) = \sum_{(b,d) \in P} g_{(b,d)}(x, y) \cdot w(b, d), \quad (1)$$

where x and y are the (x, y) -coordinates of the persistence function, $g_{(b,d)}$ is a smoothing function for $(b, d) \in P$, and $w(b, d) \geq 0$ is a non-negative weight function. A persistence function is a stable representation of a persistence diagram; persistence functions are robust to small perturbations of points in persistence diagrams (Adams et al., 2017).

The weight function $w(b, d)$ allows assigning different importance to points in persistence diagrams. For example, long-persisting features could be more important than the short-living features in some applications. In this case, one can assign heavier weights to the points far from the diagonal. Various weights have been suggested, such as weights only depend on persistence of features (Chen et al., 2015; Adams et al., 2017; Kusano et al., 2016) and birth, death, and persistence values (Berry et al., 2020). In this paper, we use the linear weight $w(b, d) = d - b$ so that heavier weights are assigned to the longer-surviving features.

Figure 7 illustrates a persistence diagram and its functional representation. The persistence function is computed using the Gaussian smoothing function $g_{(b,d)}(x, y) = \frac{\exp[-((x-b)^2 + (y-d)^2)]}{\sigma^2}$ with $\sigma = 1$ and the linear weight. For the two-dimensional pathology images, two persistence functions will be obtained: dimension zero and dimension one. We denote persistence functions of dimension 0 and 1 diagrams of subject i by X_i^0 and X_i^1 , respectively.

3 Cox Regression Model for Functional Data

A Cox proportional hazards regression (CR) model (Cox, 1972) is a commonly used model to investigate the association between patients' survival prognosis and predictor variables. The hazard function with scalar predictors Z has the form

$$h(t) = h_0(t) \exp(Z^T \gamma), \quad (2)$$

where h_0 is the baseline hazard function, $t \in [0, \tau]$ for $0 < \tau < \infty$, and $Z = (z_1, \dots, z_p)^T$ is a p -dimensional scalar predictor. We aim to conduct the FCR model that uses a set of scalar predictor γ and two functional predictors X^0 and X^1 as

$$h(t) = h_0(t) \exp\left(Z^T \gamma + \int X^0(u) \alpha(u) du + \int X^1(v) \beta(v) dv\right). \quad (3)$$

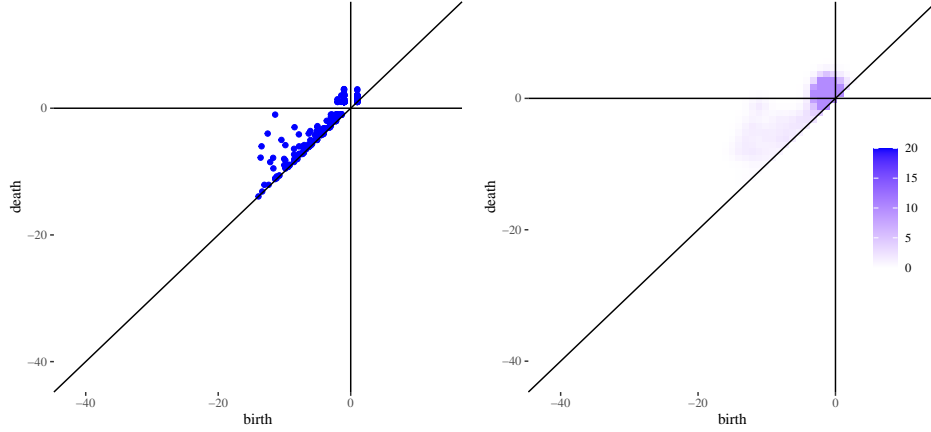


Figure 7: Persistence diagram (left) and persistence function (right).

The objective of the FCR model is to determine the unknown coefficients γ , α , and β . Due to the infinite dimensionality of functional data, dimension reduction is often required. We use the functional principal component analysis to represent functional data in a lower-dimensional space. For a review of functional data analysis, see Morris (2015); Wang et al. (2016) and references therein.

We represent the persistence functions X_i^0 and X_i^1 with a few functional principal components (FPC). Let $\mu^0(u) = E[X_i^0(u)]$ and $\mu^1(v) = E[X_i^1(v)]$ be the mean functions of X_i^0 and X_i^1 . By the spectral decomposition, the covariance functions can be represented as $\text{Cov}(X_i^0(u), X_i^0(u')) = \sum_{j=1}^{\infty} \lambda_j \phi_j(u) \phi_j(u')$ and $\text{Cov}(X_i^1(v), X_i^1(v')) = \sum_{k=1}^{\infty} \delta_k \pi_k(v) \pi_k(v')$ where $\{\lambda_j\}_{j \geq 1}$ and $\{\delta_k\}_{k \geq 1}$ are non-increasing eigenvalues and $\{\phi_j\}_{j \geq 1}$ and $\{\pi_k\}_{k \geq 1}$ are orthonormal eigenfunctions of $X_i^0(u)$ and $X_i^1(v)$. By the Karhunen-Loève theorem, the persistence functions X_i^0 and X_i^1 can be expressed as

$$X_i^0(u) = \mu^0(u) + \sum_{j=1}^{\infty} \xi_{ij} \phi_j(u),$$

$$X_i^1(v) = \mu^1(v) + \sum_{k=1}^{\infty} \zeta_{ik} \pi_k(v),$$

where $\xi_{ij} = \int (X_i^0(u) - \mu^0(u)) \phi_j(u) du$ and $\zeta_{ik} = \int (X_i^1(v) - \mu^1(v)) \pi_k(v) du$ are the FPCs of dimension zero and one, respectively. The FPCs have mean zero $E[\xi_{ij}] = E[\zeta_{ik}] = 0$ with covariances $E[\xi_{ij} \xi_{ij'}] = \lambda_j 1(j = j')$ and $E[\zeta_{ik} \zeta_{ik'}] = \delta_k 1(k = k')$ where $1(\cdot)$ is an indicator function. We can approximate functional data $X_i^0 \approx \mu^0(u) + \sum_{j=1}^q \xi_{ij} \phi_j(u)$ and $X_i^1 \approx \mu^1(v) + \sum_{k=1}^r \zeta_{ik} \pi_k(v)$, where q and r are the selected number of FPCs. Then the FCR model (3) can be approximated as

$$h_i(t) \approx h_0^*(t) \exp \left(Z_i^T \gamma + \sum_{j=1}^q \xi_{ij} \alpha_j + \sum_{k=1}^r \zeta_{ik} \beta_k \right), \quad (4)$$

where $h_0^*(t) = h_0(t) \exp(\int \mu^0(u)\alpha(u)du + \int \mu^1(v)\beta(v)dv)$. The dimension of predictors is reduced to $p + q + r$ in the FCR model (4). We can obtain the estimated coefficients using the selected FPCs and their estimated coefficients as $\hat{\alpha}(u) \approx \sum_{j=1}^q \hat{\alpha}_j \hat{\phi}_j(u)$ and $\hat{\beta}(v) \approx \sum_{k=1}^r \hat{\beta}_k \hat{\pi}_k(v)$.

Kong et al. (2018) suggest two criteria for selecting the number of FPCs for FCR models. First, the percentage of variance explained by the FPCs can be used to determine q and r . Let $PV^0(q) = \sum_{j=1}^q \lambda_j / \sum_{j=1}^{\infty} \lambda_j$ and $PV^1(r) = \sum_{k=1}^r \delta_k / \sum_{k=1}^{\infty} \delta_k$ be the percentages of variances explained by q dimension zero and r dimension one FPCs, respectively. For a given variability threshold C , the minimum number of FPCs that exceed the threshold: $q = \min\{q : PV^0(q) > C\}$ and $r = \min\{r : PV^1(r) > C\}$. Second, the Akaike information criterion (AIC) can be used to choose the number of the FPCs (Yao et al., 2005). Let $L(\gamma_1, \dots, \gamma_p, \alpha_1, \dots, \alpha_q, \beta_1, \dots, \beta_r | q, r)$ denote the partial likelihood function of the FCR (4) given the number of the FPCs q and r . The AIC value of the FCR model is $AIC(q, r) = 2(q + r) - 2 \log\{L(\hat{\gamma}_1, \dots, \hat{\gamma}_p, \hat{\alpha}_1, \dots, \hat{\alpha}_q, \hat{\beta}_1, \dots, \hat{\beta}_r | q, r)\}$. We determine an optimal number of components q and r by computing the AIC under the various combinations of q and r . For the tied event times, we use the approximation method of Efron (1977) to adjust the partial likelihood.

4 Application to Lung Cancer Data

Lung cancer is one of the most deadly cancers (Siegel et al., 2020). One of the most common types of lung cancer is adenocarcinoma that accounts for about 40% of all lung cancers (Zappa and Mousa, 2016), and it has various morphological features (Matsuda and Machii, 2015). We use 246 pathology images of 143 lung adenocarcinoma patients in the National Lung Screening Trial (NLST) data. All images are obtained under $40\times$ magnification, and the median size of images is $24,244 \times 19,261$ pixels. The images are segmented into three classes of tumor, normal, and empty regions using a deep convolutional neural network (Wang et al., 2018). We implement an additional pre-processing step to remove noise. A single pixel is considered to be noise when its class is different from the surrounding eight singular-class pixels. The noise pixels are reclassified to the class of the surrounding pixels. The denoised three-class images are transformed using SEDT-3. Figure 8 shows the denoised ternary image of Wang et al. (2018) and SEDT-3 transformed image.

A sequence of cubical complices is constructed using SEDT-3 value as filtration, and persistent homology is computed using GUDHI (Dlotko, 2015). We exclude the intervals with infinite death values to remove features related to empty regions. The median of the number of the computed features per image slice is 694 for dimension zero and 1,768 for dimension one. The ranges are $(-42, 12)$ for dimension zero and $(-20, 27)$ for dimension one persistence diagrams, respectively.

The computed persistence diagrams are represented as the persistence function by (1) using Gaussian smoothing kernel with $\sigma = 1$ and a linear weight. We observe the persistence functions

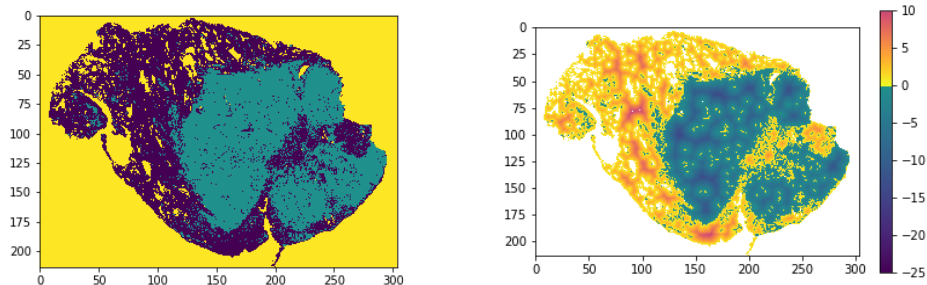


Figure 8: The denoised three-class pathology image segmented by Wang et al. (2018) (left). The SEDT-3 transformation image (right). In the SEDT-3 image, the tumor regions are colored from blue to green and the normal regions are colored yellow to red. Figures will appear in color in the electronic version of this article.

on grid points at the center of the square lattices of size one, on and above the persistence diagram’s diagonal line. As a result, we use 1,540 and 1,176 grid points for the dimension zero and one persistence functions, respectively.

We construct the CR model using the following scalar predictors: age, sex, smoking status, stage of cancer (I to IV), and tumor size. The size of tumor is measured by the number of tumor pixels in an image slice. Also, we fit the FCR model using the functional predictors and the same scalar predictors used in the CR model. The persistence functions are represented by functional principal component analysis, and FPCs are included in the model. Both the variance threshold $C = 95\%$ and the AIC criterion yield the same set of FPCs: two FPCs are selected for each dimension ($q = r = 2$). For both models, we assume the baseline hazard function $h_0(t) = 1$. The CR and FCR models are using the R-package “survival” (Therneau, 2020).

Table 1 shows the results of the CR and FCR models. Among the scalar predictors in both models, age and stage III and IV indicators have the p-values smaller than 0.05. In the FCR model, the p-values of the two FPCs are smaller than 0.05. The overall p-values of the Wald tests are 2×10^{-4} for the CR model and 3×10^{-7} for the FCR model. The scalar variables behave similarly for both models except for the tumor size predictor. The p-value of the tumor size variable is increased in the FCR model as the functional predictors are included. This suggests that one of the functional predictors may include the tumor size information.

The estimated coefficients of persistence functions, $\hat{\alpha}(u)$ and $\hat{\beta}(v)$, show which features affect the survival prognosis and how they are related. Figure 9 shows the estimated functional coefficients. The blue-colored and red-colored areas have positive and negative effects on the hazard function, respectively. Each estimated coefficient has quadrants with positive and negative effect.

The topological features recorded in the blue-colored areas in Figure 9 (quadrant III of Figure 9a and quadrant II of Figure 9b) correspond to the aggressive tumor patterns. First,

Table 1: The outputs of the Cox regression and functional Cox regression models. The ‘coef.’ and ‘SE’ are abbreviations of the coefficient and standard error, respectively. The p-values smaller than 0.05 are marked in bold.

	Cox regression model				Functional Cox regression model			
	coef.	exp(coef.)	SE	p-value	coef.	exp(coef.)	SE	p-value
age	0.084	1.088	0.023	0.007	0.084	1.087	0.024	0.013
smoking/nonsmoking	-0.067	0.935	0.262	0.831	-0.157	0.855	0.235	0.636
female/male	0.081	1.085	0.235	0.803	0.144	1.155	0.243	0.664
tumor size	0.000	1.000	0.000	0.084	0.000	1.000	0.000	0.550
stage I vs. stage II	0.545	1.725	0.382	0.366	0.608	1.837	0.389	0.307
stage I vs. stage III	1.195	3.304	0.270	0.002	1.224	3.402	0.277	0.002
stage I vs. stage IV	1.442	4.227	0.342	0.002	1.481	4.400	0.350	0.002
dimension 0, 1 st FPC	-	-	-	-	0.006	1.007	0.002	0.000
dimension 0, 2 nd FPC	-	-	-	-	0.017	1.017	0.008	0.086
dimension 1, 1 st FPC	-	-	-	-	0.002	1.002	0.001	0.055
dimension 1, 2 nd FPC	-	-	-	-	-0.012	0.988	0.004	0.001

quadrant III of Figure 9a represents the relatively small connected tumor shapes. The small connected tumor features are spotted where tumor regions overlap, or multiple normal regions are placed inside of tumor regions (i.e., see the examples of area H in Figure 6a). Similarly, the normal regions surrounded by tumor regions appear in the quadrant II of Figure 9b (i.e., see the example of the area M in Figure 6b). On the other hand, the shapes appear in the red-colored regions in Figure 9 (quadrant II of Figure 9a and quadrant I of Figure 9b) match with less aggressive tumor behaviors. First, quadrant I of Figure 9b corresponds to broken-ring shaped tumor regions (i.e., see the examples of areas N, P, and O in Figure 6a). These shapes require an ample-sized normal region that could be surrounded by tumor but not invaded by tumor. If a small tumor region penetrates the normal region inside the broken-ring shaped tumor regions, the dimension one features are not constructed. Therefore, the broken-ring shaped tumor may not likely to appear where the small tumor regions are densely populated. This corresponds to quadrant II in Figure 6a. The colored area in quadrant II has small birth values with death values a little far from zero. This area represents the small-sized scattered tumor regions with distances between the tumor regions are not that close (i.e., see the example of area B in Figure 6a). It reveals that the small tumor regions are not densely distributed, implying a slow spread of tumors. These results coincide with the findings on how the size, number, shape, and distribution of tumors associate with tumor progression and patient survival (Yokoyama et al., 1991; Miller et al., 2003; Hashiba et al., 2006; Chatzistamou et al., 2010; Vogl et al., 2013; Grove et al., 2015)

and tissue transport properties (Soltani and Chen, 2012; Sefidgar et al., 2014).

Another interesting observation is that the relatively small-sized (approximately up to 10×10 pixels) topological features have large effects on the hazard function. We see that most non-zero estimated coefficient areas (i.e., colored areas in Figure 9) are close to the origin compared to the ranges of persistence functions. The topological features near the origin correspond to small-sized features; they have small birth and death values. This indicates that the valuable information obtained by the proposed persistent homology approach is local shapes and patterns.

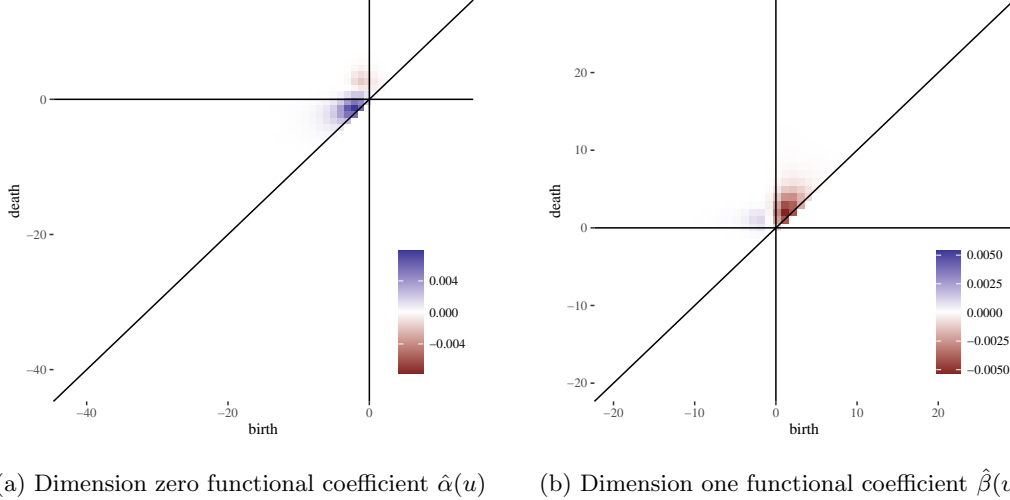


Figure 9: Estimated coefficient functions $\hat{\alpha}(u)$ and $\hat{\beta}(v)$ of the functional Cox linear regression model. Figures will appear in color in the electronic version of this article.

4.1 Topological Feature Validation Test

We conduct a hypothesis test to check the validity of topological features for predicting the survival outcome. The coefficients of functional data $\alpha(u)$ and $\beta(v)$ are, we can conduct the hypothesis using a few basis

$$\begin{aligned}
 H_0 : \quad & \alpha_1 = \alpha_2 = \dots = \alpha_q = \beta_1 = \dots = \beta_r = 0 \\
 H_1 : \quad & \alpha_j \neq 0 \text{ or } \beta_k \neq 0 \text{ for at least one } j \in \{1, 2, \dots, q\} \text{ or } k \in \{1, 2, \dots, r\}.
 \end{aligned}$$

For the proposed FCR model of pathology images, we conduct the chi-square test of degrees of freedom four because four functional basis are selected ($q = r = 2$). The computed p-value is 8×10^{-14} , suggesting that the topological features are a strong signal. Aside from the clinical (scalar) variables included in the model, the topological features offer additional information in predicting lung cancer patients' survival outcomes.

4.2 Prediction using Cross-validation

We predict the risk scores using the leave-one-out cross-validation for two models, the CR model (2) and FCR model (4). For a given pathology image $I \in \{1, 2, \dots, 246\}$, the models are trained for the rest 245 images. The risk score of I is predicted using the trained model. We repeat it for all 246 images, and the predicted risk scores are averaged for each patient. We assign the patients into two groups of 71 high-risk patients and 72 low-risk patients using the median patient-wise risk score.

Figure 10 presents the Kaplan-Meier plots of high- and low-risk groups predicted by the two models. The proposed FCR model shows a better separation between the two groups over the CR model. The p-value of the log-rank test of the FCR model is 2×10^{-7} , which is smaller than that of the CR model 2×10^{-4} .

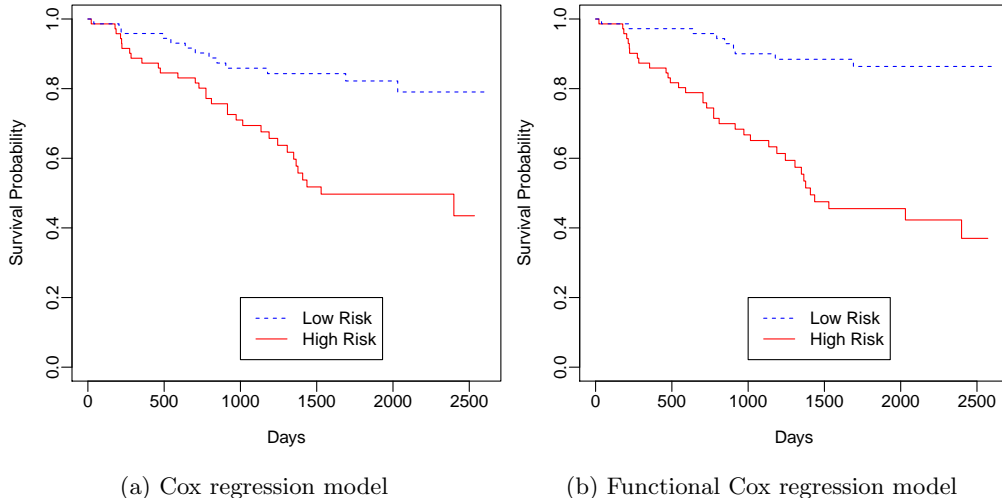


Figure 10: The Kaplan–Meier plots for the low and high risk groups of the null and functional Cox linear regression models

5 Discussion

In this article, we propose a new summary statistic to represent the shape of tumor pathology images using their topological features. We develop the distance transform for three-class pathology images to reveal various tumor patterns. We use persistent homology to quantify shape information and provide potential clinical interpretation of computed topological features. The topological persistence information is represented as functional data and used to fit the FCR model to predict the survival prognosis of lung adenocarcinoma patients. The topological features are shown to have a significant non-zero effect on the hazard function. Also, the topological signals improve the predictive accuracy over the CR model. This suggests that the

topological features well summarize tumor aggressiveness.

Our study leads to several interesting topics for future research. While we found a relationship between the topological shape features and survival prognosis, a complex relationship between the shape features, clinical variables, and genetic features are largely unknown. Recent studies investigate the relationships between imaging features and gene expressions; using the radiomic features of pancreatic ductal adenocarcinoma (Li et al., 2019) and the degree of tumor eccentricity of breast cancer (Moon et al., 2015). The future research topic will include exploring the association of topological shape features with gene expressions. One of the drawbacks of the proposed persistent homology approach is that it loses tumor location information. This is suitable for the lung adenocarcinoma application that the images do not have a pre-determined direction. However, the tumor spatial information could be important in some cancer image analyses, such as brain tumor (Bondy et al., 2008). In the future, it would be useful to pair spatial information with the topological features computed by persistent homology. Also, we use the entire image slice, although the image size varies from 61×72 to 335×578 and the ratios of empty regions are different. Although we adjust the scale by including the size of tumor in the FCR model, it would be interesting to develop scale-standardization methods for topological features. Section 4 shows that the topological features related to the hazard function are small-sized. It would be interesting to investigate whether the sampled image patches also contain the small-sized feature information and how they affect survival predictions.

References

- Adams, H., Emerson, T., Kirby, M., Neville, R., Peterson, C., Shipman, P., Chepushtanova, S., Hanson, E., Motta, F., and Ziegelmeier, L. (2017), “Persistence Images: A Stable Vector Representation of Persistent Homology,” *Journal of Machine Learning Research*, 18, 1–35.
- Bendich, P., Chin, S. P., Clark, J., Desena, J., Harer, J., Munch, E., Newman, A., Porter, D., Rouse, D., Strawn, N., and Watkins, A. (2016), “Topological and statistical behavior classifiers for tracking applications,” *IEEE Transactions on Aerospace and Electronic Systems*, 52, 2644–2661.
- Berry, E., Chen, Y.-C., Cisewski-Kehe, J., and Fasy, B. T. (2020), “Functional summaries of persistence diagrams,” *Journal of Applied and Computational Topology*, 4, 211–262.
- Bharath, K., Kurtek, S., Rao, A., and Baladandayuthapani, V. (2018), “Radiologic image-based statistical shape analysis of brain tumours,” *Journal of the Royal Statistical Society: Series C (Applied Statistics)*, 67, 1357–1378.
- Bianconi, F., Fravolini, M. L., Bello-Cerezo, R., Minestrini, M., Scialpi, M., and Palumbo, B.

- (2018), “Evaluation of shape and textural features from CT as prognostic biomarkers in non-small cell lung cancer,” *Anticancer research*, 38, 2155–2160.
- Bondy, M. L., Scheurer, M. E., Malmer, B., Barnholtz-Sloan, J. S., Davis, F. G., Il’Yasova, D., Kruchko, C., McCarthy, B. J., Rajaraman, P., Schwartzbaum, J. A., et al. (2008), “Brain tumor epidemiology: consensus from the Brain Tumor Epidemiology Consortium,” *Cancer*, 113, 1953–1968.
- Bookstein, F. L. (1997), *Morphometric tools for landmark data: geometry and biology*, Cambridge University Press.
- Brú, A., Casero, D., De Franciscis, S., and Herrero, M. A. (2008), “Fractal analysis and tumour growth,” *Mathematical and Computer Modelling*, 47, 546–559.
- Bubenik, P. (2015), “Statistical Topological Data Analysis Using Persistence Landscapes,” *Journal of Machine Learning Research*, 16, 77–102.
- Carlsson, G. (2009), “Topology and data,” *Bulletin of the American Mathematical Society*, 46, 255–308.
- Chatzistamou, I., Rodriguez, J., Jouffroy, T., Girod, A., Point, D., Sklavounou, A., Kittas, C., Sastre-Garau, X., and Klijanienko, J. (2010), “Prognostic significance of tumor shape and stromal chronic inflammatory infiltration in squamous cell carcinomas of the oral tongue,” *Journal of Oral Pathology & Medicine*, 39, 667–671.
- Chazal, F., Fasy, B., Lecci, F., Michel, B., Rinaldo, A., Rinaldo, A., and Wasserman, L. (2017), “Robust Topological Inference: Distance to a Measure and Kernel Distance,” *Journal of Machine Learning Research*, 18, 5845–5884.
- Chen, K., Chen, K., Müller, H.-G., and Wang, J.-L. (2011), “Stringing high-dimensional data for functional analysis,” *Journal of the American Statistical Association*, 106, 275–284.
- Chen, Y.-C., Wang, D., Rinaldo, A., and Wasserman, L. (2015), “Statistical Analysis of Persistence Intensity Functions,” *arXiv e-prints*.
- Coupric, M., Bezerra, F.-N., and Bertrand, G. (2001), “Topological operators for grayscale image processing,” *Journal of Electronic Imaging*, 10, 1003 – 1015.
- Cox, D. R. (1972), “Regression Models and Life-Tables,” *Journal of the Royal Statistical Society. Series B (Methodological)*, 34, 187–220.
- Crawford, L., Monod, A., Chen, A. X., Mukherjee, S., and Rabadán, R. (2020), “Predicting clinical outcomes in glioblastoma: an application of topological and functional data analysis,” *Journal of the American Statistical Association*, 115, 1139–1150.

- Dlotko, P. (2015), “Cubical complex,” in *GUDHI User and Reference Manual*, GUDHI Editorial Board.
- Dryden, I. L. and Mardia, K. V. (2016), *Statistical shape analysis: with applications in R*, vol. 995, John Wiley & Sons.
- Edelsbrunner, H. and Harer, J. (2008), “Persistent Homology - a Survey,” *Contemporary mathematics*, 453, 257–282, Surveys on Discrete and Computational Geometry: Twenty Years Later. Providence, IMS.
- Efron, B. (1977), “The Efficiency of Cox’s Likelihood Function for Censored Data,” *Journal of the American Statistical Association*, 72, 557–565.
- Gellar, J. E., Colantuoni, E., Needham, D. M., and Crainiceanu, C. M. (2015), “Cox regression models with functional covariates for survival data,” *Statistical Modelling*, 15, 256–278.
- Gillies, R. J., Kinahan, P. E., and Hricak, H. (2016), “Radiomics: images are more than pictures, they are data,” *Radiology*, 278, 563–577.
- Grove, O., Berglund, A. E., Schabath, M. B., Aerts, H. J., Dekker, A., Wang, H., Velazquez, E. R., Lambin, P., Gu, Y., Balagurunathan, Y., et al. (2015), “Quantitative computed tomographic descriptors associate tumor shape complexity and intratumor heterogeneity with prognosis in lung adenocarcinoma,” *PloS one*, 10, e0118261.
- Hao, M., Liu, K.-y., Xu, W., and Zhao, X. (2020), “Semiparametric Inference for the Functional Cox Model,” *Journal of the American Statistical Association*, 1–11.
- Haralick, R. M., Shanmugam, K., and Dinstein, I. (1973), “Textural Features for Image Classification,” *IEEE Transactions on Systems, Man, and Cybernetics*, SMC-3, 610–621.
- Hashiba, T., Hashimoto, N., Maruno, M., Izumoto, S., Suzuki, T., Kagawa, N., and Yoshimine, T. (2006), “Scoring radiologic characteristics to predict proliferative potential in meningiomas,” *Brain tumor pathology*, 23, 49–54.
- Herring, A. L., Robins, V., and Sheppard, A. P. (2019), “Topological persistence for relating microstructure and capillary fluid trapping in sandstones,” *Water Resources Research*, 55, 555–573.
- Kilday, J., Palmieri, F., and Fox, M. D. (1993), “Classifying mammographic lesions using computerized image analysis,” *IEEE transactions on medical imaging*, 12, 664–669.
- Kong, D., Ibrahim, J. G., Lee, E., and Zhu, H. (2018), “FLCRM: Functional linear cox regression model,” *Biometrics*, 74, 109–117.

- Kovalevsky, V. (1989), “Finite topology as applied to image analysis,” *Computer Vision, Graphics, and Image Processing*, 46, 141 – 161.
- Kusano, G., Hiraoka, Y., and Fukumizu, K. (2016), “Persistence weighted Gaussian kernel for topological data analysis,” *Proceedings of The 33rd International Conference on Machine Learning*, 48, 2004–2013.
- Lawson, P., Sholl, A., Brown, J., Fasy, B. T., and Wenk, C. (2019), “Persistent Homology for the Quantitative Evaluation of Architectural Features in Prostate Cancer Histology,” *Scientific Reports*, 9, 1139.
- Lee, E., Zhu, H., Kong, D., Wang, Y., Sullivan Giovanello, K., Ibrahim, J. G., and Neuroimaging Initiative, f. t. A. D. (2015), “BFLCRM: A Bayesian functional linear Cox regression model for predicting time to conversion to Alzheimer’s disease,” *Annals of Applied Statistics*, 9, 2153–2178.
- Li, K., Xiao, J., Yang, J., Li, M., Xiong, X., Nian, Y., Qiao, L., Wang, H., Eresen, A., Zhang, Z., et al. (2019), “Association of radiomic imaging features and gene expression profile as prognostic factors in pancreatic ductal adenocarcinoma,” *American journal of translational research*, 11, 4491.
- Lopes, R., Ayache, A., Makni, N., Puech, P., Villers, A., Mordon, S., and Betrouni, N. (2011), “Prostate cancer characterization on MR images using fractal features,” *Medical physics*, 38, 83–95.
- Madabhushi, A. and Lee, G. (2016), “Image analysis and machine learning in digital pathology: Challenges and opportunities,” *Medical image analysis*, 33, 170–175.
- Matsuda, T. and Machii, R. (2015), “Morphological distribution of lung cancer from Cancer Incidence in Five Continents Vol. X,” *Japanese Journal of Clinical Oncology*, 45, 404–404.
- Miller, T. R., Pinkus, E., Dehdashti, F., and Grigsby, P. W. (2003), “Improved prognostic value of 18F-FDG PET using a simple visual analysis of tumor characteristics in patients with cervical cancer,” *Journal of Nuclear Medicine*, 44, 192–197.
- Moon, C., Mitchell, S. A., Heath, J. E., and Andrew, M. (2019), “Statistical inference over persistent homology predicts fluid flow in porous media,” *Water Resources Research*, 55, 9592–9603.
- Moon, H.-G., Kim, N., Jeong, S., Lee, M., Moon, H., Kim, J., Yoo, T.-K., Lee, H.-B., Kim, J., Noh, D.-Y., et al. (2015), “The clinical significance and molecular features of the spatial tumor shapes in breast cancers,” *PloS one*, 10, e0143811.

- Morris, J. S. (2015), “Functional Regression,” *Annual Review of Statistics and Its Application*, 2, 321–359.
- Oyama, A., Hiraoka, Y., Obayashi, I., Saikawa, Y., Furui, S., Shiraishi, K., Kumagai, S., Hayashi, T., and Kotoku, J. (2019), “Hepatic tumor classification using texture and topology analysis of non-contrast-enhanced three-dimensional T1-weighted MR images with a radiomics approach,” *Scientific Reports*, 9, 1–10.
- Qaiser, T., Sirinukunwattana, K., Nakane, K., Tsang, Y.-W., Epstein, D., and Rajpoot, N. (2016), “Persistent Homology for Fast Tumor Segmentation in Whole Slide Histology Images,” *Procedia Computer Science*, 90, 119 – 124.
- Qu, S., Wang, J.-L., and Wang, X. (2016), “Optimal estimation for the functional Cox model,” *Ann. Statist.*, 44, 1708–1738.
- Rangayyan, R. M., El-Faramawy, N. M., Desautels, J. L., and Alim, O. A. (1997), “Measures of acutance and shape for classification of breast tumors,” *IEEE Transactions on medical imaging*, 16, 799–810.
- Reininghaus, J., Huber, S. M., Bauer, U., and Kwitt, R. (2015), “A stable multi-scale kernel for topological machine learning,” *2015 IEEE Conference on Computer Vision and Pattern Recognition*, 4741–4748.
- Rizzo, S., Botta, F., Raimondi, S., Origgi, D., Fanciullo, C., Morganti, A. G., and Bellomi, M. (2018), “Radiomics: the facts and the challenges of image analysis,” *European radiology experimental*, 2, 1–8.
- Robins, V., Saadatfar, M., Delgado-Friedrichs, O., and Sheppard, A. P. (2016), “Percolating length scales from topological persistence analysis of micro-CT images of porous materials,” *Water Resources Research*, 52, 315–329.
- Sefidgar, M., Soltani, M., Raahemifar, K., Bazmara, H., Nayinian, S. M. M., and Bazargan, M. (2014), “Effect of tumor shape, size, and tissue transport properties on drug delivery to solid tumors,” *Journal of biological engineering*, 8, 12.
- Siegel, R. L., Miller, K. D., and Jemal, A. (2020), “Cancer statistics, 2020,” *CA: A Cancer Journal for Clinicians*, 70, 7–30.
- Soltani, M. and Chen, P. (2012), “Effect of tumor shape and size on drug delivery to solid tumors,” *Journal of biological engineering*, 6, 4.
- Therneau, T. M. (2020), *A Package for Survival Analysis in R*, R package version 3.1-12.

- Turner, K., Mukherjee, S., and Boyer, D. M. (2014), “Persistent homology transform for modeling shapes and surfaces,” *Information and Inference: A Journal of the IMA*, 3, 310–344.
- Vogl, T. J., Worst, T. S., Naguib, N. N., Ackermann, H., Gruber-Rouh, T., and Nour-Eldin, N.-E. A. (2013), “Factors influencing local tumor control in patients with neoplastic pulmonary nodules treated with microwave ablation: a risk-factor analysis,” *American journal of roentgenology*, 200, 665–672.
- Wang, J.-L., Chiou, J.-M., and Müller, H.-G. (2016), “Functional Data Analysis,” *Annual Review of Statistics and Its Application*, 3, 257–295.
- Wang, S., Chen, A., Yang, L., Cai, L., Xie, Y., Fujimoto, J., Gazdar, A., and Xiao, G. (2018), “Comprehensive analysis of lung cancer pathology images to discover tumor shape and boundary features that predict survival outcome,” *Scientific Reports*, 8, 10393.
- Yao, F., Müller, H.-G., and Wang, J.-L. (2005), “Functional Data Analysis for Sparse Longitudinal Data,” *Journal of the American Statistical Association*, 100, 577–590.
- Yokoyama, I., Sheahan, D., Carr, B., Kakizoe, S., Selby, R., Tzakis, A., Todo, S., Iwatsuki, S., and Starzl, T. (1991), “Clinicopathologic factors affecting patient survival and tumor recurrence after orthotopic liver transplantation for hepatocellular carcinoma,” *Transplantation Proceedings*, 23, 2194–2196.
- Zappa, C. and Mousa, S. A. (2016), “Non-small cell lung cancer: current treatment and future advances,” *Translational lung cancer research*, 5, 288.